International Journal of Applied Earth Observation and Geoinformation 146 (2026) 105141

Contents lists available at ScienceDirect

International Journal of Applied Earth Observation and Geoinformation

journal homepage: www.elsevier.com/locate/jag

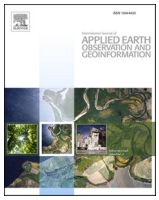

Exploring the impacts of dual-polarized vegetation indices and U-shaped deep learning architectures on SAR-based burned area mapping☆

S.M. Sohel Rana [a], Jaese Lee [a,b], Yoojin Kang [c], Jungho Im [a,d,e,*]

[a] Department of Civil, Urban, Earth and Environmental Engineering, Ulsan National Institute of Science and Technology, Ulsan, Republic of Korea
[b] Department of Environment and Energy Engineering, Gwangju Institute of Science and Technology, Gwangju, Republic of Korea
[c] Department of Forestry, Environment, and Systems, Kookmin University, Seoul, Republic of Korea
[d] Graduate School of Carbon Neutrality, Ulsan National Institute of Science and Technology, Ulsan, Republic of Korea
[e] Graduate School of Artificial Intelligence, Ulsan National Institute of Science and Technology, Ulsan, Republic of Korea

ARTICLE INFO

Keywords:
Burned Area Mapping
SAR
Vegetation Indices
U-Net++
Log-Ratio

ABSTRACT

Frequent and severe wildfires driven by climate change intensify the need for accurate burned area (BA) mapping, which can be effectively addressed using Synthetic Aperture Radar (SAR) due to its cloud-penetration capability and sensitivity to vegetation and moisture changes. However, BA mapping based on SAR-only approaches relies on U-Net with ResNet50 backbone or fully convolutional neural network, while the potential of advanced architectural components remains underexplored. Moreover, prior research primarily emphasizes log-ratio features, with limited focus on standalone capacity of dual polarized vegetation indices (VIs). This study addresses these gaps by evaluating the performance of five U-Net variants (U-Net, Attention U-Net, Residual Attention U-Net, U-Net++, and U-Net 3 +) using four input schemes: log-ratio, log-ratio without cross-ratio, VIs, and a combined feature set of all. Three combinations of loss function such as binary cross entropy (BCE), dice, and focal are also applied to the best model of all scheme. Experimental results show that U-Net++ with log-ratio inputs under BCE loss function achieves the highest performance, yielding an F1 score of 0.8218 and an Intersection of Union (IoU) of 0.6795. Further analysis reveals that VIs alone can effectively delineate burned areas (F1: 0.8244; IoU: 0.7013) with focal loss, and combining them with log-ratio features delivers the best performance (F1: 0.8364; IoU: 0.7188), when dice and focal loss functions are applied. Overall, this study offers a quantitative evaluation of how dual-polarized VIs and deep learning architectures affect SAR-based BA mapping performance and suggests promising directions for future enhancement through advanced feature extraction techniques.

1. Introduction

Global climate change is driving warmer, drier conditions, leading to more frequent and severe wildfires worldwide (Kondylatos et al., 2022; Pechony and Shindell, 2010). While fires often benefit ecosystems by promoting biodiversity and regeneration (Keeley et al., 2011), its increasing severity has devastating effects (Bowman et al., 2020), including impacts on forest recovery (Jenkins et al., 2011; Jin et al., 2012; Li and Xu, 2023). Therefore, accurate burned area (BA) mapping is essential for estimating biomass loss, assessing ecological damage, informing fire prediction and post-fire management, and evaluating socio-economic impacts (Bowman et al., 2009; Pausas and Keeley, 2009; Van der Werf et al., 2010). Remote sensing, especially satellite optical data such as Landsat and Sentinel-2, plays a key role in BA mapping due to its spectral sensitivity in detecting burn scars (Quintano et al., 2018; Ramayanti et al., 2024). However, their performance is limited to the cases with cloud cover, smoke, or shadows (Sudmanns et al., 2019).

Active sensors like synthetic aperture radar (SAR) overcome these limitations by acquiring data through clouds and smoke, day or night, regardless of lighting conditions (Chuvieco et al., 2019; Kobayashi et al., 2024). Though more complex to interpret, SAR is highly complementary to optical data for BA mapping as researchers have persistently explored its potential (Bourgeau-Chavez et al., 2002). SAR-based burned area mapping relies on detecting changes in radar backscatter caused by fire-induced alterations in vegetation, soil structure, and moisture, which affect surface dielectric properties and typically reduce backscatter

☆ This article is part of a special issue entitled: 'Remote Sensing of Wildfires' published in International Journal of Applied Earth Observation and Geoinformation.

* Corresponding author.
E-mail address: ersgis@unist.ac.kr (J. Im).

https://doi.org/10.1016/j.jag.2026.105141
Received 30 April 2025; Received in revised form 12 September 2025; Accepted 29 January 2026
Available online 3 February 2026

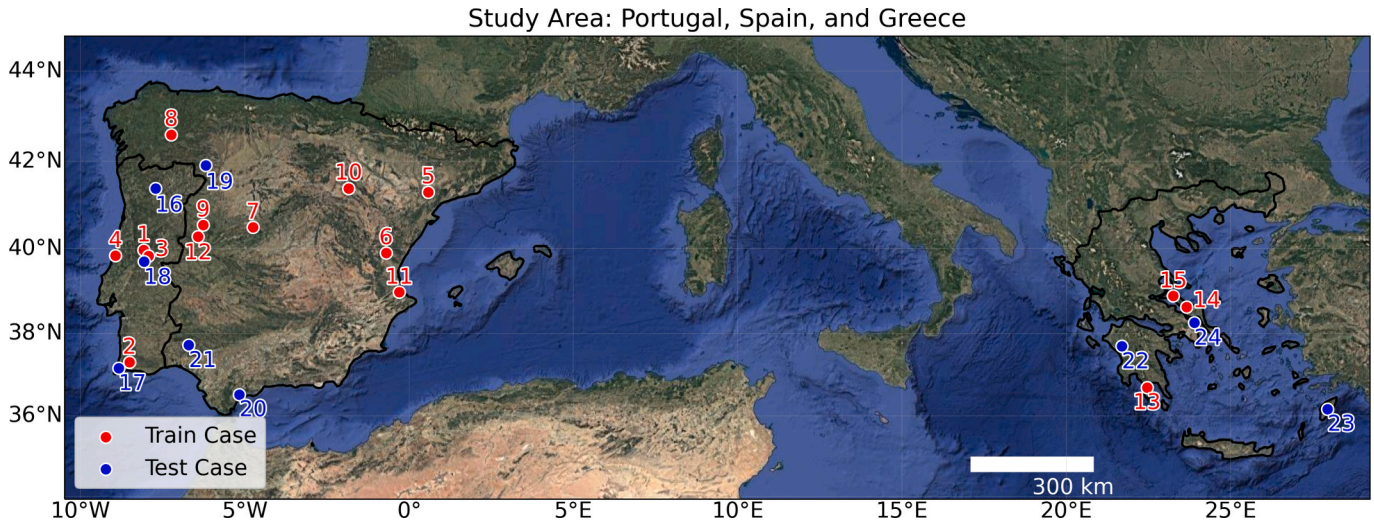

Fig. 1. Distribution of training and testing wildfire cases across the three countries of Europe (The numbers are from table 1).

Table 1
List of fire cases and their ignition start and end time according to Copernicus emergency management service (EMS) rapid mapping information.

No	Area	Country	Fire Start	Fire End	Data Usage
1	Predógão Grande	Portugal	2017.06.17	2017.06.20	Train & Validation
2	Monchique	Portugal	2018.08.03	2018.08.10	
3	Ermida	Portugal	2020.07.25	2020.07.28	
4	Marinha Grande	Portugal	2017.10.15	2017.10.17	
5	La Torre de l'Espanyol	Spain	2019.06.26	2019.06.30	
6	Bejís	Spain	2022.08.13	2022.08.20	
7	Ávila	Spain	2021.08.14	2021.08.19	
8	Folgoso do Courel	Spain	2022.07.15	2022.07.23	
9	Ladrillar	Spain	2022.07.11	2022.07.19	
10	Moros	Spain	2022.07.18	2022.7.20	
11	La Drova	Spain	2018.08.06	2018.08.11	
12	Pinofranqueado	Spain	2023.05.17	2023.05.19	
13	Drosopigi	Greece	2020.08.22	2020.08.25	
14	Makrimalli	Greece	2019.08.13	2019.08.21	
15	Evia	Greece	2021.08.03	2021.08.13	
16	Vilarinho de Samarda	Portugal	2022.08.21	2022.08.24	Test
17	Barao de Sao Joao	Portugal	2020.06.19	2020.06.21	
18	Vila de Rei	Portugal	2019.07.20	2019.07.24	
19	Sierra de la Culebra	Spain	2022.06.15	2022.06.25	
20	Jubrique	Spain	2021.09.08	2021.09.16	
21	Patras	Spain	2020.08.27	2022.08.30	
22	Ancient Olympia	Greece	2021.08.04	2021.08.17	
23	Salakos	Greece	2023.07.18	2023.07.28	
24	Kalamos	Greece	2017.08.11	2017.08.18	

intensity (Ban et al., 2020; Ruiz-Ramos et al., 2018; Zhang et al., 2019). Over the last decades, studies have explored various SAR frequencies and polarizations for BA mapping using techniques like backscatter differencing (Verhegghen et al., 2016), coherence analysis (Tanase et al., 2010), and polarimetric indices (Engelbrecht et al., 2017).

Traditional approaches often struggle to capture the spatial complexity of post-fire effects. In contrast, machine learning (ML) models, especially convolutional neural networks—have shown great potential in learning spatial features for more accurate BA delineation (Belenguer-Plomer et al., 2021; Lee et al., 2024; Lee et al., 2023; Seo et al., 2023). SAR-based BA mapping studies with deep learning (DL) particularly used fully convolutional neural network or U-Net with ResNet50 backbone (Ban et al., 2020; Belenguer-Plomer et al., 2021; Luft et al., 2022; Radman et al., 2023; Zhang et al., 2023; Zhang et al., 2024). Among these, U-Net that incorporated total variation regularization showed improvement in cases where masks were generated from SAR images while optical reference-based model did not show additional enhancement (Zhang et al., 2023).

However, several limitations remain in previous SAR-based BA mapping studies. First, most U-Net-based studies utilized data obtained from Google Earth Engine, which often lacks terrain flattening that can enhance classification accuracy, especially in rugged terrains (Dostalova et al., 2022). Second, some studies incorporated images one month after the fire, limiting early mapping (Zhang et al., 2024). Furthermore, although alternative features such as the radar burn difference, the dual polarization SAR vegetation index (Radman et al., 2023), and the K-map (Zhang et al., 2023) have been used to enhance the performance of BA mapping, but vegetation indices performance either not improved the model and their individual contributions have not been systematically evaluated for the model performance. Also, in the vegetation indices based study (Radman et al., 2023), model was trained for each specific case instead of training for whole dataset which limits the understanding of generalized application of using indices. Besides, studies still heavily rely on the log-ratio due to its simplicity.

Therefore, two research gaps can be explored: 1) whether vegetation indices (VIs) are sufficient to delineate the burned area compared to the log-ratio, and 2) whether improvement in the U-Net structure can capture fine details compared to the original U-Net structure. SAR-based vegetation indices, including the radar vegetation index (RVI) and the bi-temporal radar forest degradation index (RFDI), have been investigated in the literature for forest change detection and biomass growth assessment (Chang et al., 2018; Periasamy, 2018). Prior studies have demonstrated that both RVI and RFDI exhibit strong correlations with optical vegetation indices, such as the normalized difference vegetation index (NDVI) (Alvarez-Mozos et al., 2021). As indices such as RFDI are specifically tailored for forest degradation detection where it captures subtle forest structure changes (e.g., partial canopy scorching), it is anticipated to offer a more nuanced representation of burned areas. Furthermore, none of the studies examined attention mechanisms (Attention U-Net) or enhanced skip connections (UNet++, UNet 3 +) that are effective in capturing fine details crucial for burned area mapping. Given that SAR-based applications including landslide detection (Dang et al., 2024; Niu et al., 2022) and flooded area mapping (Ghosh et al., 2024; Jiang et al., 2022) have demonstrated significant performance gains of the attention mechanism and redesign of the U-Net structure, the enhanced U-Net structure is expected to improve the accuracy of BA mapping.

This study aimed to demonstrate the capacity of radar VIs and improved U-Net model structures to efficiently estimate the burned area

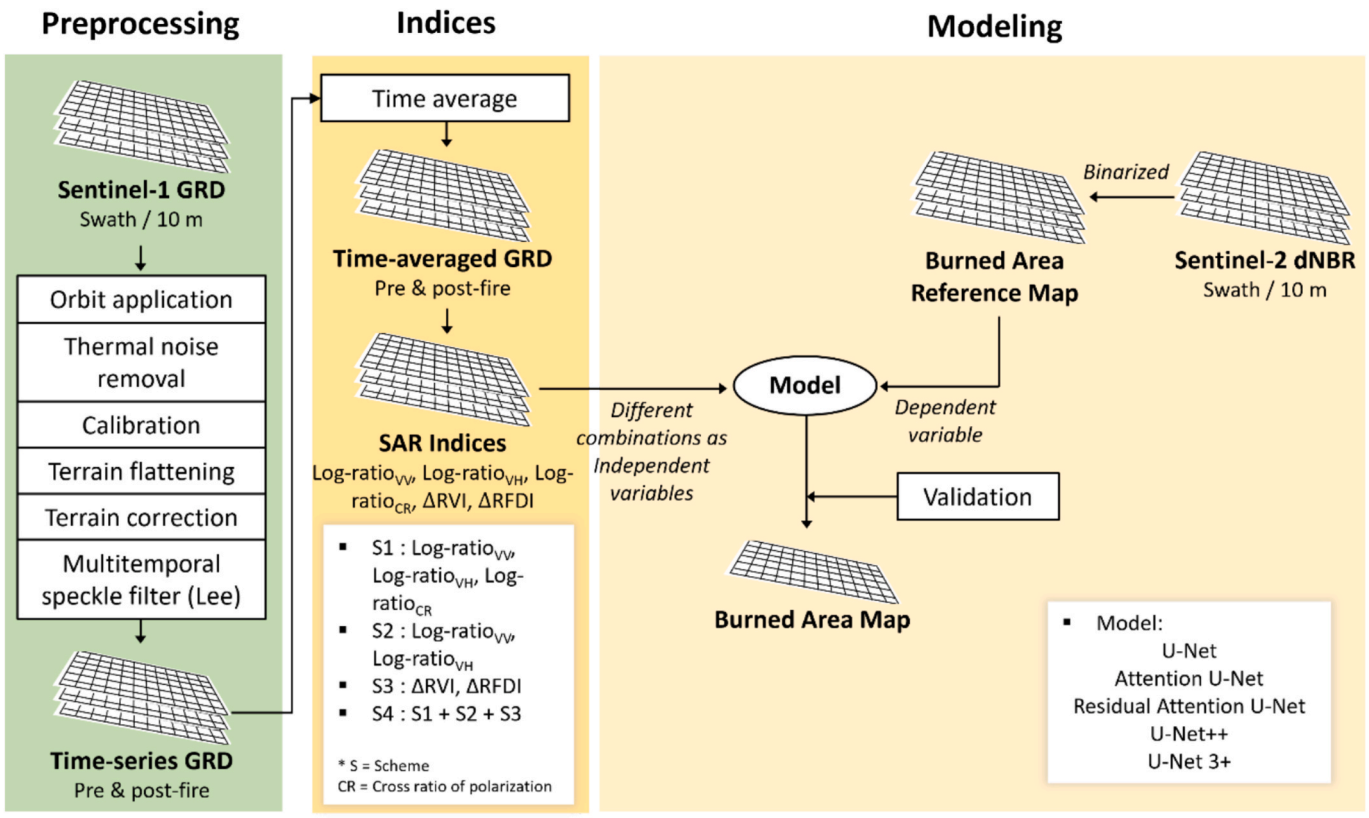

Fig. 2. Methodological workflow for burned-area mapping. Sentinel-1 GRD data were pre-processed and used to derive SAR indices under four schemes. These indices served as inputs to deep-learning models, while Sentinel-2 dNBR provided the reference burned-area maps for validation.

Table 2
Four schemes with different schemes of indices as input channels for burned area mapping.

Scheme	Input indices	No. of channels
1	Log-ratio$_{VV}$, Log-ratio$_{VH}$, CR	3
2	Log-ratio$_{VV}$, Log-ratio$_{VH}$	2
3	*ΔRVI, ΔRFDI*	2
4	Log-ratio$_{VV}$, Log-ratio$_{VH}$, CR, *ΔRVI, Δ RFDI*	5

Table 3
Comparison of the performance of different models (bold values indicate the best performance in each column).

Model	OA	Precision	Recall	F1-score	IoU
U-Net (ResNet50)	0.9392	0.8637	0.7476	0.8015	0.6687
U-Net	0.9378	0.8609	0.7412	0.7966	0.6620
Attention U-Net	0.9411	0.8484	0.7812	0.8134	0.6855
Residual Attention U-Net	0.9413	0.8303	0.8079	0.8190	0.6934
U-Net++	**0.9428**	0.8420	0.8025	**0.8218**	**0.6975**
U-Net 3+	0.9367	0.7981	**0.8225**	0.8101	0.6808

using Sentinel-1 SAR data. The specific objective of the study is to identify the usefulness of dual polarization radar VIs in SAR-based BA mapping compared to log-ratio and to quantify the capacity of the attention mechanism and redesigned skip connection in the U-shaped models to BA mapping accuracy.

Table 4
Comparison of performance and computational characteristics of the evaluated models.

Model	F1-score	FLOPs (GFLOPs)	Params (M)	Model size	Inference time
U-Net	0.7966	54.71	31.04 M	178.42 MB	8.5698
Attn. U-Net	0.8134	83.78	40.45 M	163.31 MB	10.3154
Attn. Res. U-Net	0.8190	58.54	32.79 M	141.21 MB	9.9231
U-Net++	0.8218	135.14	35.29 M	134.61 MB	16.8365
U-Net 3 Plus	0.8101	199.81	26.99 M	103.01 MB	29.0498

2. Materials and methods

2.1. Study area

For this study, 24 wildfire events were selected across Spain (7 sites), Portugal (11 sites), and Greece (6 sites), covering a broad range of vegetation types, topographic settings, and fire severities to support generalizable findings (Fig. 1). The selected wildfires span a temporal range from 2017 to 2023, offering a comprehensive dataset for analysis. Among them, 15 cases were selected for training and validation and 9 for testing the generalization ability of the developed models (Table 1). To avoid potential biases due to class imbalance and to ensure representative sampling in the validation set, the data were grouped into four bins based on the ratio of burned to unburned areas: 0% (no burned pixels), 1–30%, 31–60%, and greater than 60%. Validation samples were then drawn from each bin, preserving a broader distribution of burned and unburned instances.

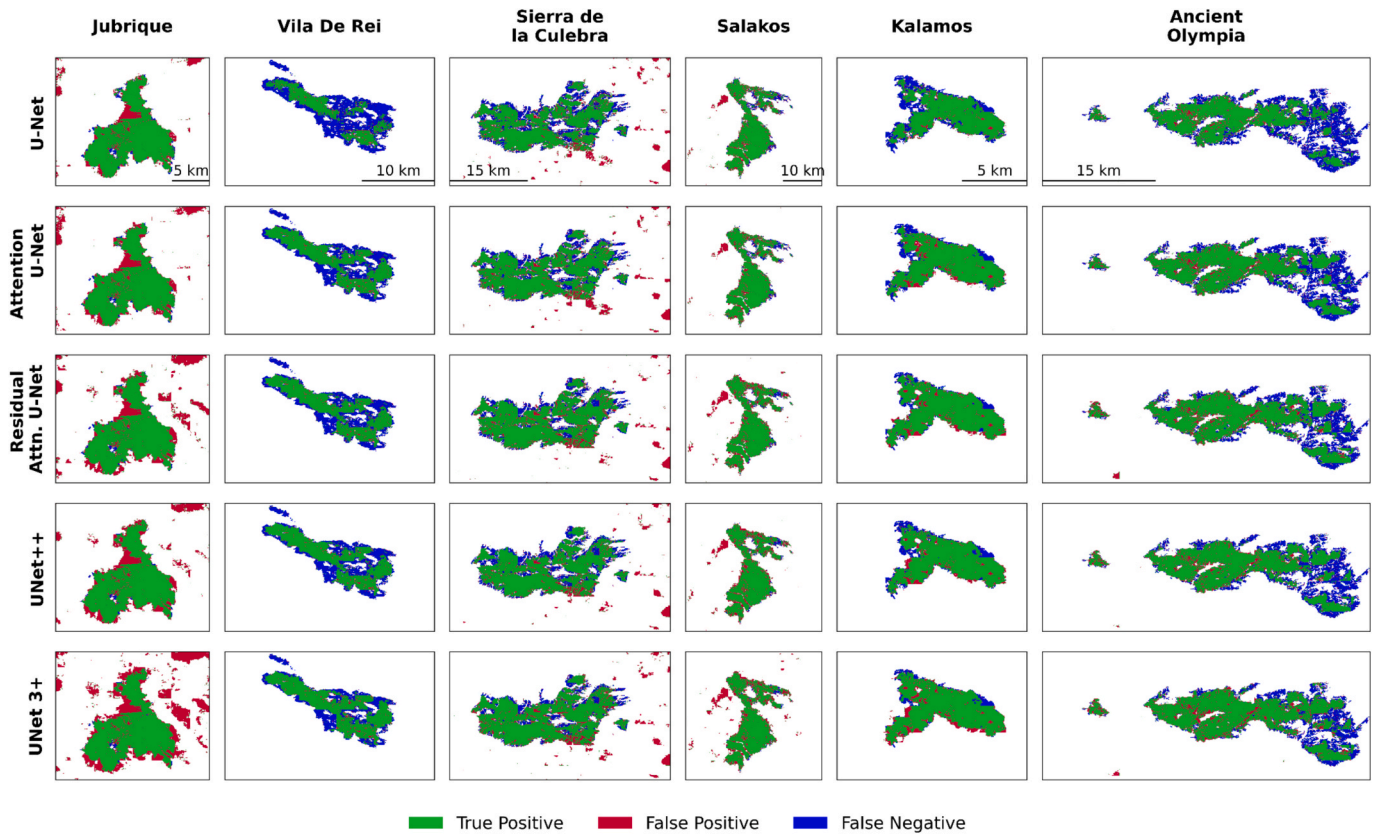

Fig. 3. The prediction of different models for scheme 1 input features in 6 of the 9 test areas.

Table 5
Comparison between the different loss functions by scheme for the best model U-Net++.

Scheme	Loss function	OA	Precision	Recall	F1-score	IoU
1	BCE	0.9428	0.8420	0.8025	0.8218	0.6975
	Dice	0.9403	0.8218	0.8126	0.8172	0.6909
	Focal	0.9418	0.8443	0.7920	0.8173	0.6911
	Dice + Focal	0.9409	0.8220	0.8173	0.8197	0.6944
2	BCE	0.9410	0.8231	0.8163	0.8197	0.6945
	Dice	0.9407	0.8321	0.8008	0.8162	0.6895
	Focal	0.9392	0.8121	0.8194	0.8157	0.6888
	Dice + Focal	0.9402	0.8077	0.8349	0.8211	0.6965
3	BCE	0.9387	0.7997	0.8364	0.8176	0.6915
	Dice	0.9362	0.7771	0.8575	0.8153	0.6882
	Focal	0.9430	0.8349	0.8142	0.8244	0.7013
	Dice + Focal	0.9371	0.7755	0.8689	0.8195	0.6942
4	BCE	0.9456	0.8760	0.7793	0.8248	0.7019
	Dice	0.9452	0.8389	0.8248	0.8318	0.7121
	Focal	0.9468	0.8805	0.7820	0.8284	0.7070
	Dice + Focal	0.9477	0.8603	0.8137	0.8364	0.7188

2.2. Sentinel-1

Sentinel-1 is the C-band SAR mission operated by the European Commission and European Space Agency, currently with two constellations 1A and 1C. While there was Sentinel 1B, but it was decommissioned in 2022 due to an anomaly. The satellite provides data in four modes, namely, interferometric wide swath (IW), extra wide swath, wave, and stripmap with single or multi-polarization depending on the mode (Torres and Davidson, 2019). This study utilizes IW mode Ground Range Detected (GRD) with dual polarization (VH and VV) and both ascending and descending orbit products. The spatial resolution of the Sentinel-1 GRD product is 20 m × 22 m (ground range x azimuth), with a pixel spacing of 10 m x10 m (ground range x azimuth). The data had been downloaded from Alaska Satellite Facilities (https://search.asf.alaska.edu/).

2.3. Experimental setup

This study designed a structured workflow integrating Sentinel-1 and Sentinel-2 data preprocessing, index derivation, segmentation model configuration, and training settings to evaluate burned area mapping (Fig. 2).

The processing of Sentinel-1 followed the preprocessing flow outlined in De Luca et al. (2021). Sentinel-1 GRD data were preprocessed in ESA SNAP (v9.0.4) with Snappy Python. The preprocessing steps included applying the orbit file, removing thermal noise, conducting radiometric calibration to β_0, performing radiometric terrain flattening, correcting terrain using the SRTM DEM, and converting β_0 to γ_0. A multi-temporal speckle filtering technique (5 × 5 Lee filter) was subsequently applied to stacked images. For each wildfire, all acquisitions occurred one month prior to the event and the earliest post-fire images from both ascending and descending passes were processed. Averages for VH and VV polarizations before and after the fire were computed, leading to the derivation of four polarimetric indices: log-ratio for VV and VH polarization, cross ratio (CR), radar vegetation index (RVI), and radar forest degradation index (RFDI). Additionally, their temporal differences (ΔRVI, ΔRFDI) were calculated. Four input schemes, combining three indices with 2 to 5 channels, were evaluated (Table 2).

We evaluated the U-Net model along with four variants: Attention U-Net, Residual Attention U-Net, U-Net++, and U-Net3 + for burned-area mapping. U-Net (Ronneberger et al., 2015) is widely utilized in remote sensing due to its encoder–decoder structure, which features skip connections that facilitate precise localization while maintaining contextual awareness (Badrinarayanan et al., 2017). Attention U-Net (Oktay, 2018) adds attention gates to highlight relevant features, while Residual

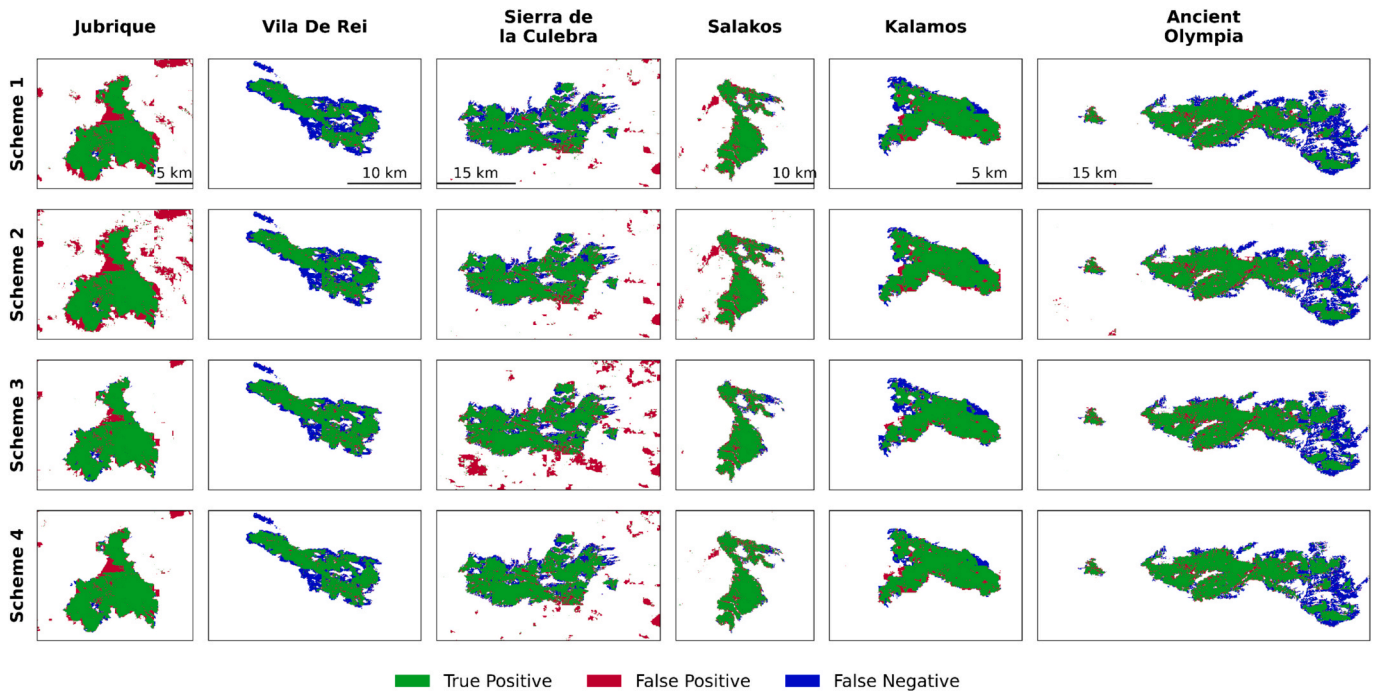

Fig. 4. Burned area mapping with different input schemes.

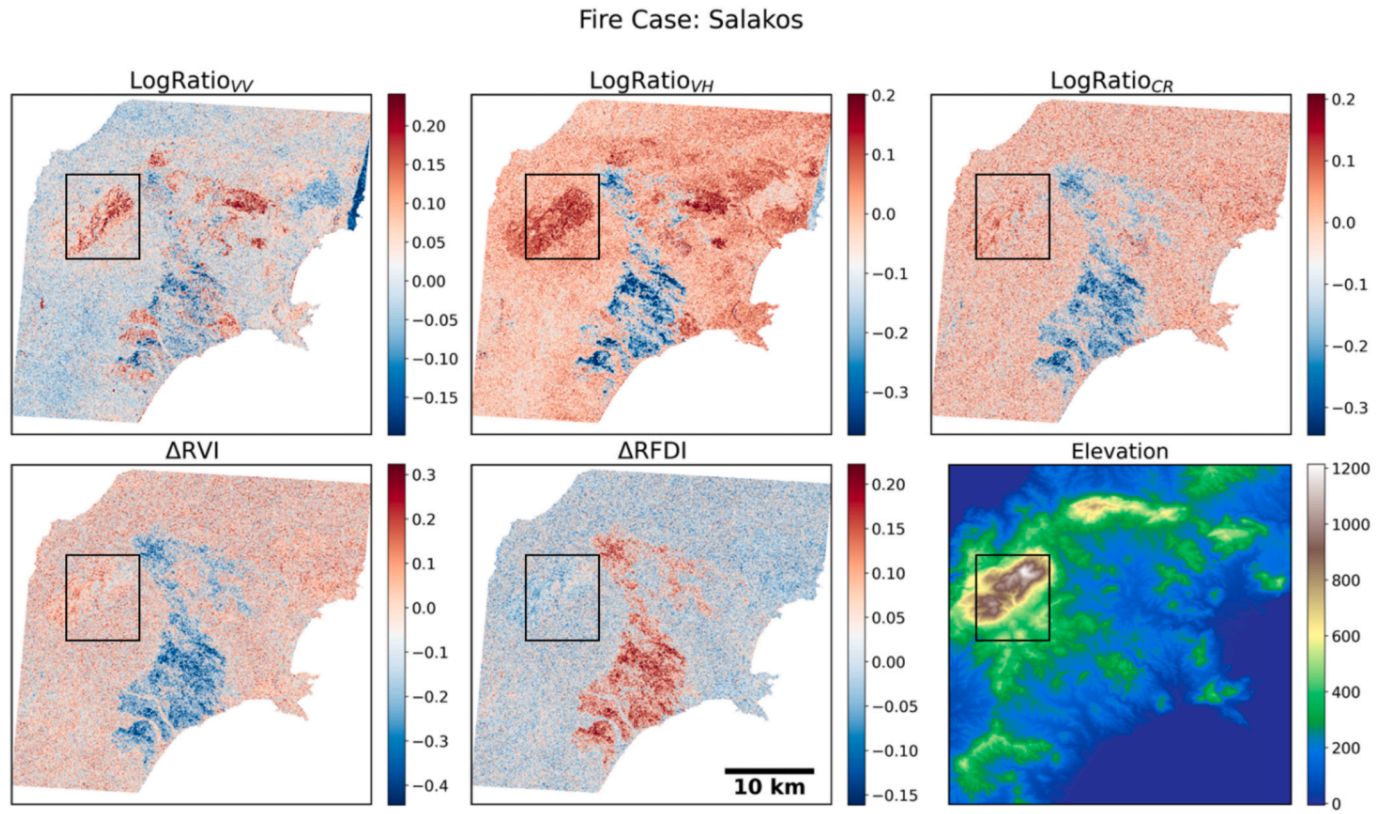

Fig. 5. Comparison of polarization indices across study site with terrain flattening effects. The black box highlights a region where high elevation and DEM resolution limitations produce Log-ratio$_{VV}$ values similar to burned areas, while ΔRVI and ΔRFDI indices show less susceptibility to these terrain-induced false positives.

Attention U-Net (John and Zhang, 2022) incorporates residual learning to support deeper training. U-Net++ (Zhou et al., 2019) utilizes dense skip connections along with deep supervision, and U-Net3+ (Huang et al., 2020) employs multi-scale feature fusion to improve contextual understanding. In our experiments, we modified U-Net++ to start with 64 channels in the first convolutional layer, rather than the standard 32.

The models were trained on an NVIDIA RTX 3090 with 24 GB memory, utilizing the Adam optimizer (Kingma and Ba, 2015) with a learning rate of 0.001, a batch size of 8. During the training process, He initialization and batch normalization were implemented. To address

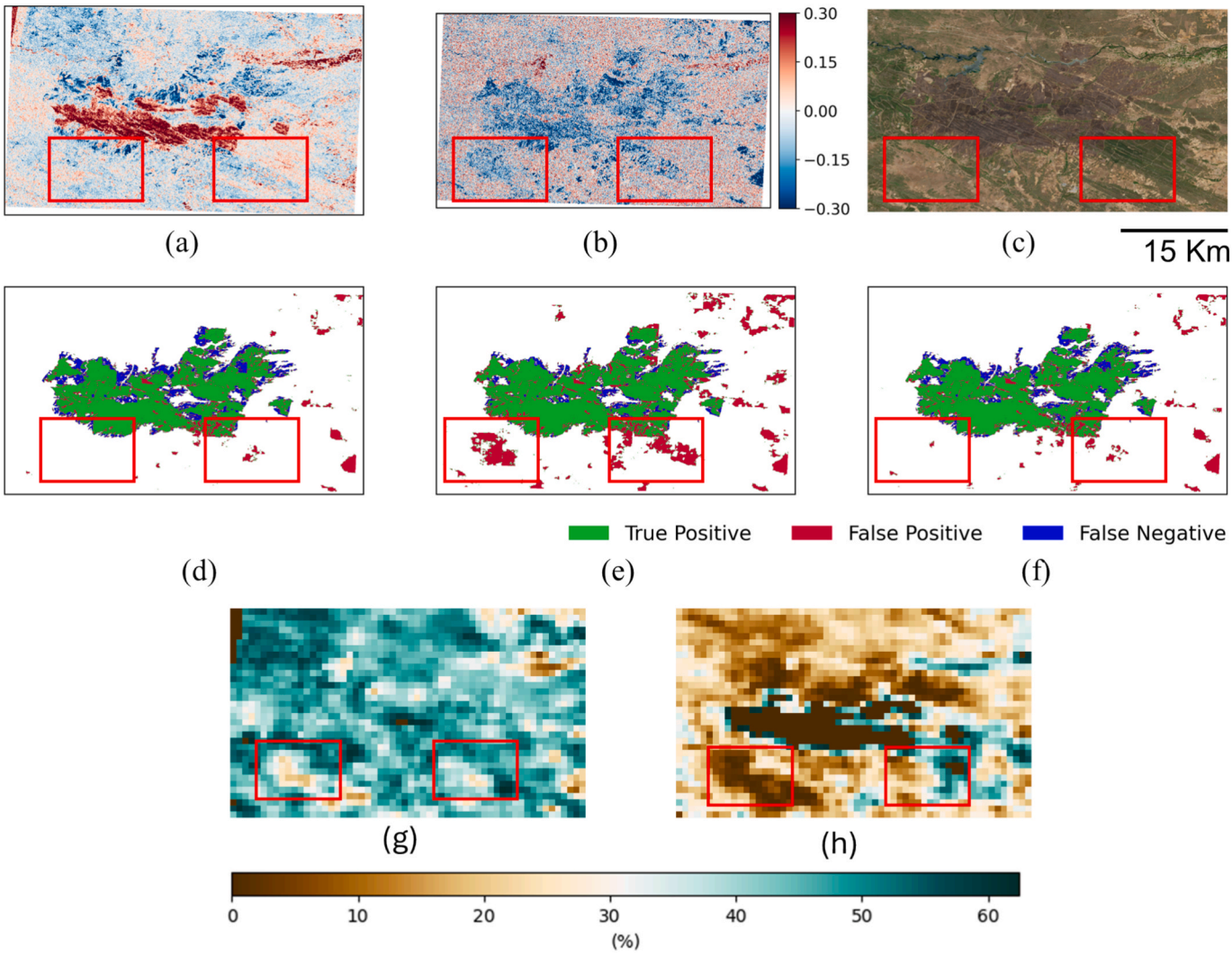

Fig. 6. Land cover and scheme comparison for the Sierra de la Culebra wildfire: (a) Log-ratio$_{VV}$, (b) ΔRVI, (c) post-fire Sentinel-2 true color composite, (d) Scheme 1 result, (e) Scheme 3 result, (f) Scheme 4 result, (g) pre-fire soil moisture, and (h) post-fire soil moisture. The red box highlights barren areas in the study site. (For interpretation of the references to colour in this figure legend, the reader is referred to the web version of this article.)

class imbalance, several loss functions were assessed, including binary cross-entropy (BCE), dice loss, and focal loss ($\alpha = 0.5$, $\gamma = 2$), as well as combinations of dice and focal losses. The training spanned 50 epochs and incorporated early stopping with a patience parameter of 10, in addition to checkpointing on the best validation loss. The decision to train for 50 epochs was consistent with values reported in previous studies (Zhang et al., 2023). A learning rate scheduler was employed to reduce the rate by a factor of 0.1 if validation loss plateaued for four consecutive epochs. Model outputs were binarized at a threshold of 0.5.

For the comprehensive analysis of U-Net and its variants with input variable schemes for BA mapping, we conducted our experiment as follows:

- Step 1: All models were first compared using input scheme 1.
- Step 2: The optimal model from step 1 was then assessed with all input schemes and loss functions.
- Step 3: Final evaluations examined wildfire-specific performance across the test set.

3. Reference data processing

Sentinel-2-based binarized differenced Normalized Burn Ratio (dNBR) has been used as reference data for this study. Among the 13 bands of Sentinel-2, band 8A and 12 were used to calculate the dNBR following equations 7 and 8. dNBR is widely adopted as a reference layer in burned area mapping studies, especially in regions or circumstances where good quality official data is not available (Ban et al., 2020; Kurum, 2015; Tanase et al., 2015; Zhang et al., 2019).

$$dNBR = \frac{(\text{Band 8A} - \text{Band 12})}{(\text{Band 8A} + \text{Band 12})} \quad (1)$$

$$dNBR = prefireNBR - postfireNBR \quad (2)$$

Two Sentinel-2 images from the pre- and post-fire periods were processed in Google Earth Engine. The dNBR was clipped to the study area, reprojected, and resampled to 10 m to align with the Sentinel-1 GRD product. Following Key and Benson (2006), a threshold of 0.1 was applied to binarize burned and unburned areas. To minimize noise, we removed irrelevant regions using the fire perimeter provided by the Copernicus EMS. This perimeter is derived from very high-resolution imagery (e.g., 1–3 m), which enhances the reliability of the ground truth in the Copernicus EMS product. Our analysis was performed at a spatial resolution of 10 m, utilizing both the reference from Sentinel-2 imagery and the Sentinel-1 GRD product.

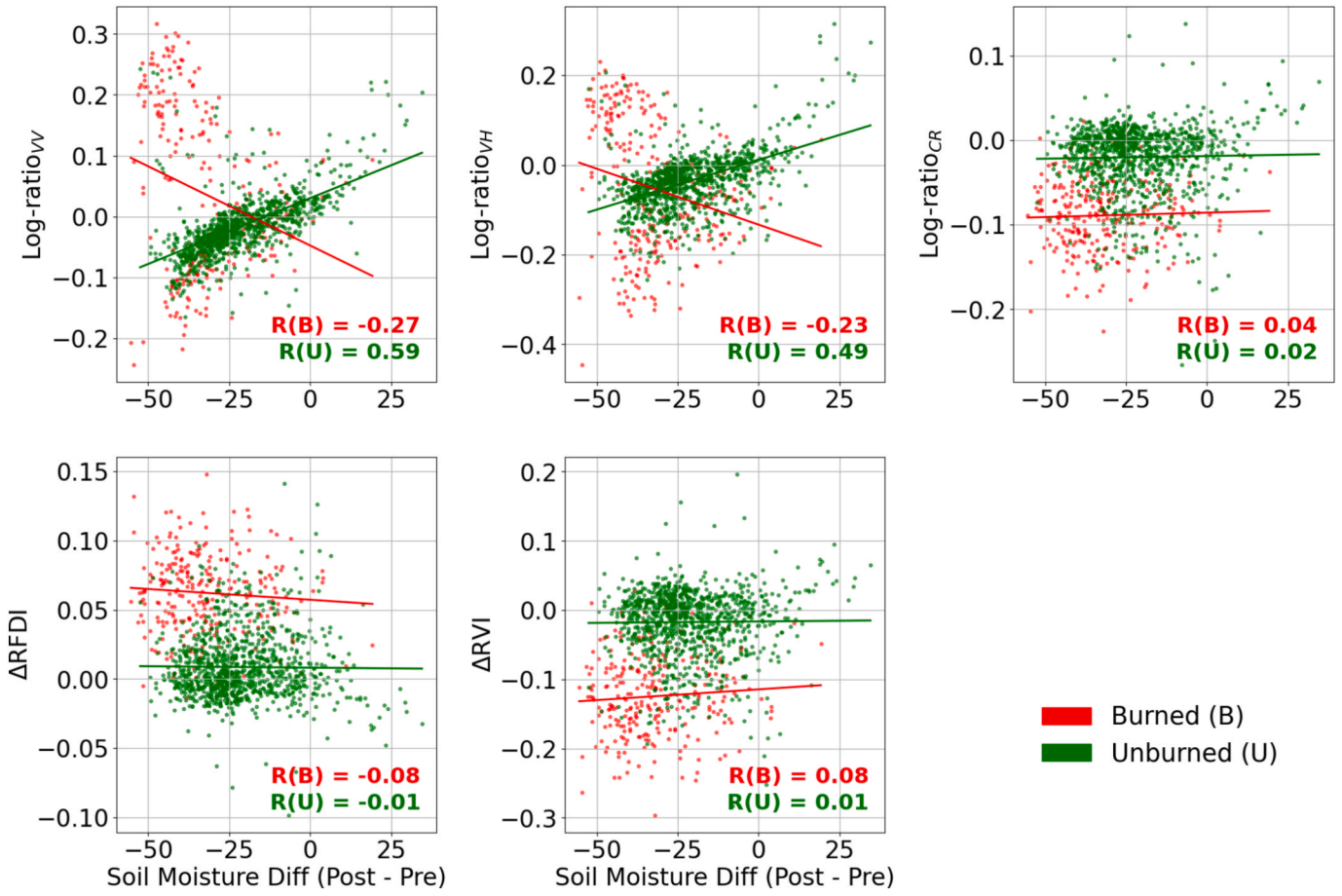

Fig. 7. Scatter plots showing the relationship between soil moisture difference (post-fire minus pre-fire) and various SAR-based and vegetation indices (Log-ratio$_{VV}$, Log-ratio$_{VH}$, Log-ratio$_{CR}$, ΔRFDI, ΔRVI). Data points are color-coded by burn status: red for burned (B) and green for unburned (U). Linear regression lines are shown for each group, with R^2 values for the full dataset (All), burned (B), and unburned (U) regions. The results highlight differing moisture relationships with SAR indices in burned versus unburned areas, while vegetation indices show more uniform trends. (For interpretation of the references to colour in this figure legend, the reader is referred to the web version of this article.)

3.1. Model evaluation

Several widely used metrics, including overall accuracy (OA), precision, recall, f1-score and total intersection over union (IoU), were employed to comprehensively assess the quality of the burned area maps (equations 3–7). OA represents the proportion of correctly classified pixels (burned and unburned) compared to reference data (Boschetti et al., 2004). While OA provides a general measure of performance, it does not differentiate between errors of omission (unburned areas mapped as burned) and commission (burned areas mapped as unburned). To address this limitation, precision and recall metrics were calculated. Precision measures the proportion of correctly identified burned pixels out of all pixels mapped as burned, while recall quantifies the proportion of actual burned pixels that were correctly identified by the algorithm (Padilla et al., 2015). High precision indicates low commission errors, whereas a high recall implies low omission errors. Furthermore, the F1-score has been computed, which is the harmonic mean of precision and recall, providing a single metric that balances both measures (Goutte and Gaussier, 2005). The F1-score ranges from 0 to 1, with higher values indicating better overall performance in terms of minimizing both omission and commission errors. IoU measures the overlap between predicted burned pixels and the corresponding reference pixels, relative to their union. This metric thus provides a robust indicator of how accurately the model captures the extent of burned areas. In a binary setting, the total IoU is computed by averaging the IoU values for both classes (burned and unburned), yielding a balanced assessment of the model's segmentation quality.

$$\text{Precision} = \frac{\text{TP}}{(\text{TP} + \text{FP})} \tag{3}$$

$$\text{Recall} = \frac{\text{TP}}{(\text{TP} + \text{FN})} \tag{4}$$

$$\text{Overall Accuracy (OA)} = \frac{\text{TP}}{(\text{TP} + \text{FP})} \tag{5}$$

$$\text{F1} - \text{score} = \frac{2 \times \text{Recall} \times \text{Precision}}{\textit{Precision} + \text{Recall}} \tag{6}$$

$$\text{IoU} = \frac{\text{TP}}{(\text{TP} + \text{FP} + \text{FN})} \tag{7}$$

where TP, FP, TN, and FN denote true positive, false positive, true negative, and false negative, respectively.

4. Results

4.1. Evaluation of the models

In this experiment, we take scheme 1 as the baseline input features, as they are the most widely used for BA mapping and BCE as the default loss function. The U-Net++ showed the best F1-score of 0.8218 and IoU of 0.6975 for the test dataset compared to the second-best Residual

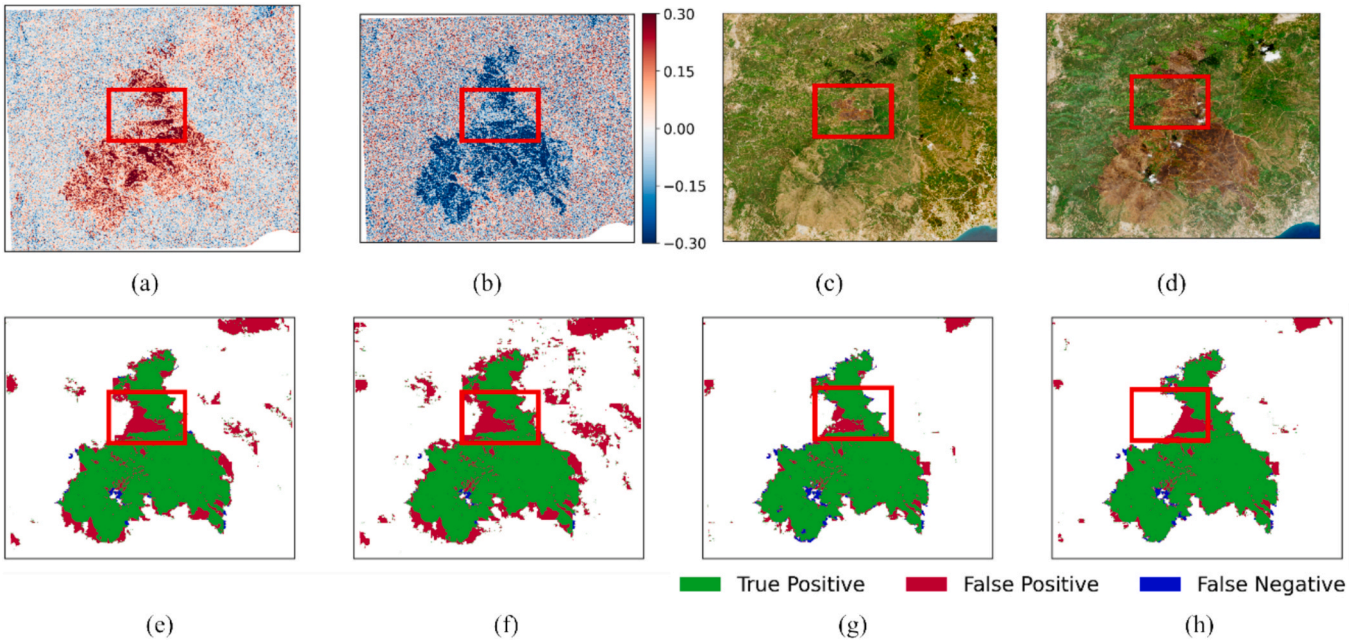

Fig. 8. Model performance in the previously burned scar for the Jurbique study case (a) Log-ratio$_{VV}$ (b) ΔRVI (c) Pre fire Sentinel 1 True color composite (d) post fire Sentinel 2 true color composite (e)-(h) represents the result from schemes 1 to 4 best results, respectively. Red mark zone in the center highlights the previously burned scar. (For interpretation of the references to colour in this figure legend, the reader is referred to the web version of this article.)

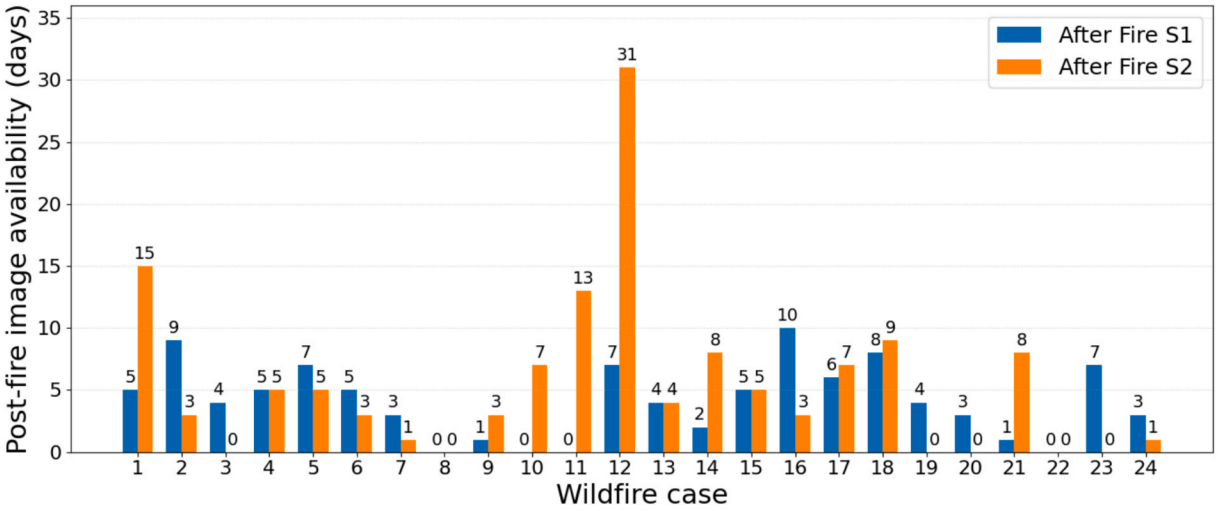

Fig. 9. Availability of Sentinel-1 and Sentinel-2 images for the wildfire cases analyzed in this study. The values in y-axis indicate the number of days after the fire event until the first available post-fire image. The values for the wildfire case in x-axis correspond to those reported in Table 1.

Attention U-Net with an F1-score of 0.8190 (Table 3). Models such as Attention U-Net and U-Net3 + have F1-scores over 0.81, while U-Net achieved 0.7966. This highlighted that the attention mechanism and the redesigned skip connections improved the BA mapping performance compared to the U-Net model. Considering the OA, every model had a metric value over 0.93. Notably, the U-Net++ model had a good balance between precision (0.8420) and recall (0.8025), while the other models exhibited a tradeoff between precision and recall.

Table 4 summarizes the FLOPs, the number of parameters, model size, and total inference time. U-Net++ performed the best with compensation of the inference time. Attn. Res. U-Net performed similarly with slightly less F1-score, but with higher efficiency in the inference time. In contrast, U-Net showed the highest efficiency, but the lowest performance.

Fig. 3 demonstrates that U-Net++ exhibits fewer false positives than the other models. However, for the Vila De Rei site (second column of Fig. 3), all models demonstrated a relatively high number of false negatives. Among these, U-Net and Attention U-Net performed poorly, whereas Residual Attention U-Net and U-Net++ yielded better results (Fig. 3). Across the Jubrique (Fig. 3) and Vilarinho De Samarda (Fig. S1) test sites, U-Net++ demonstrated substantially better predictions with fewer false positives compared to other models. Although the Residual Attention U-Net achieved good separability for Salakos, U-Net++ still outperformed it overall (Fig. 3).

4.2. *Input feature schemes & loss functions*

Following the best results in Section 3.1, we further analyzed the effects of input feature schemes against U-Net++. The hyperparameters for training were the same for different schemes. Scheme 4, which

includes a scheme of all the indices and log-ratio, performed slightly higher in F1-score and IoU compared to other schemes (Table 5).

As the dataset was imbalanced between burned and unburned areas (Fig. S2), different loss functions (dice, focal, and dice + focal) were evaluated in addressing the class imbalance for each scheme (Table 5). The results showed that the dice loss alone did not improve the performance of the model except for scheme 4. Scheme 1 exhibited the best performance with the default BCE loss function. The combination of dice and focal loss improved the performance of scheme 2 with an increase in recall, but precision was compromised. For scheme 3, focal loss improved the model performance with a higher F1-score (0.8244) and IoU (0.6965) with balanced precision and recall (0.8349 and 0.8142, respectively). Overall, the best model is the scheme 4 with the dice and focal loss combined, resulting in the best F1-score value of 0.8364 and total IoU value of 0.7188.

This indicates that leveraging all available indices along with the log-ratio features and training with both dice and focal losses best addressed the class imbalance and boosted BA detection. The higher F1-score for scheme 3 compared to log-ratio schemes (2 and 4) also highlighted better performance can be achieved with vegetation indices alone.

4.3. Qualitative analysis for test cases

In this section, we compared the spatial distribution of test cases for each scheme's best model, focusing on the balance between FP and FN predictions (Fig. 4). Overall, schemes 3 and 4 exhibited fewer FP outcomes. Wildfire events such as Jubrique and Vila De Rei performed better for scheme 3, whereas Vilarinho de Samarda (Fig. S3) was best modeled by scheme 4. In the Jubrique case, schemes 1 and 2 were noisier (i.e., more FP), while schemes 3 and 4 substantially reduced FP errors, suggesting that the used of additional indices in the input features enhanced model performance. Conversely, Vila De Rei suffered from higher FN rates for schemes 1 and 2, while scheme 3 improved outcomes. However, scheme 4 produced more FN than scheme 3 for this particular wildfire.

Salakos shows fewer FN predictions under scheme 3 compared to schemes 1, 2, and 4, but scheme 4 demonstrates more accurate edge detection of the burned area. For Vilarinho de Samarda, schemes 1 and 2 yield decent results, although scheme 3 increases FP predictions. Scheme 4 demonstrates a better FP–FN balance, a trend also observed in Barao de Sao Joao and Kalamos (where FN rates are minimal) and Sierra de la Culebra (where FP classification is notably reduced).

Cases like Patras (Fig. S3) and Ancient Olympia (Fig. 4), all the four models show similar results with scheme 4 has less FP results. Consequently, scheme 4 emerges as the most robust approach overall, indicating that leveraging a comprehensive set of spectral indices alongside log-ratio features provides the most reliable burned-area estimations in terms of mitigating both FP and FN errors.

5. Discussion

This study demonstrates that the U-Net++ architecture outperforms other U-Net variants when using log-ratio inputs for burned area (BA) mapping. The combination of log-ratio features with VIs, alongside a combined dice and focal loss function, yielded the highest overall performance. Notably, VIs alone, when paired with a suitable loss function such as focal loss, performed competitively, suggesting their potential in cases where log-ratio inputs may be ambiguous or less effective. Comparative analysis revealed that ResNet50 backbones improve performance relative to standard U-Net, corroborating findings by Luft et al. (2022) and Zhang et al. (2021). However, U-Net++ provided the most consistent gains, attributable to its nested skip connections, which facilitate progressive feature refinement and enhance boundary preservation, critical in SAR-based segmentation where edge delineation is often noisy and complex (Zhou et al., 2019). While U-Net 3 + introduces more extensive skip connections, it did not yield further improvement in this context, suggesting its architectural design may be less compatible with the characteristics of SAR data.

Predictions from all models of schemes 1 and 2, particularly in cases like Salakos and Jubrique, reveal that they exhibit FP in particular place of the area, whereas scheme 3 demonstrates notably refined performance, surpassing even that of scheme 4 (Figs. 3 and 4). This might be related to the terrain flattening characteristics and the usefulness of the dual polarization indices (Fig. 5). Although the dataset is terrain flattened but the combination of high elevation, relatively low-resolution Digital Elevation Model (DEM) data from SRTM, and variations in incident angle produces (Fig. S5) values in Log-ratio$_{VV}$ that closely resemble those of burned areas as can be seen in the black box zone in Fig. 5. This pattern is notably less pronounced in polarimetric indices such as ΔRVI and ΔRFDI. The results suggest that scheme 3, with its reduced sensitivity to terrain-induced false positives, performs better in these challenging topographic conditions. In contrast, schemes incorporating all variables still misclassify these regions as burned areas, primarily driven by the misleading log-ratio$_{VV}$ component. These findings indicate two potential paths for improvement: either implementing higher-resolution DEM data to address topographic correction errors or preferentially utilizing polarimetric indices for more accurate burned area delineation. The latter approach may offer a more practical solution when high-resolution elevation data is unavailable.

Barren land and previously burned areas can negatively affect burned area detection, particularly when relying solely on VIs. In regions such as Sierra de la Culebra, barren land exhibited similar responses to burned areas particularly in indices such as ΔRVI, resulting in false positives (Fig. 6). Soil moisture data from the Copernicus surface soil moisture product (Bauer-Marschallinger et al., 2018) suggest that this confusion may be associated with changing soil moisture to lower value, as areas with reduced moisture exhibited backscatter patterns comparable to those of recently BA (Fig. 6g and 6h).

Also, from the red boxed area in Fig. 6, the correlation (Fig. 7) shows that the relationship between burned and unburned regions in the log-ratio and VIs are different. Specifically, the log-ratio (VV and VH) exhibit opposing relationships with soil moisture in burned and unburned regions, indicating a negative correlation divergence. In contrast, VIs, i.e. ΔRVI, display similar directional responses to soil moisture across both classes, suggesting that VIs alone may lack the discriminatory sensitivity to capture the nuanced hydrological changes introduced by fire disturbance. These imply that log-ratio indices may inherently reflect structural or dielectric changes associated with burning more distinctly, making them potentially superior in identifying burned-related soil moisture anomalies. The consistent response of VIs across burned and unburned zones highlights a limitation in their specificity, which can be mitigated by integrating soil moisture data as a complementary variable in predictive modeling frameworks. Future studies could include soil moisture data in the model or adjust the use of VIs based on the moisture levels for each area.

Previously burned areas also presented challenges, as their backscatter signals often resembled those of low-severity current burns, reducing model performance (Fig. 8). Enhanced temporal modeling or the use of post-fire vegetation recovery indicators may offer a path forward.

Several challenges must be considered when implementing the approach applied in this study. As described in Section 2.3, imagery from up to one month prior to ignition, along with at least one ascending and one descending post-fire acquisition, was used. This strategy of averaging pre-fire images over one month reduces noise, as suggested by De Luca et al. (2021). Using a single post-fire image per orbit ensures timely burned-area estimation with reduced latency. As shown in Fig. 9, Sentinel-1 acquisitions were available earlier than Sentinel-2 for most wildfire cases, underscoring the critical role of SAR in providing the first reliable post-fire observations when optical imagery was delayed or cloud-obscured. Furthermore, the use of both ascending and descending orbit images is essential, as reliance on a single orbit may increase

errors, as previously noted by Engelbrecht et al. (2017). In some cases, such as Ancient Olympia and Vila De Rei, accurately mapping BA may be nearly impossible due to the absence of discernible signals in the SAR images, despite the use of advanced DL or ML models. Similar limitations were highlighted by Paluba et al. (2024), emphasizing that SAR-based burned area mapping can be unreliable in certain scenarios where fire-induced changes are minimal or obscured.

Our methodological workflow is structured as a semi-automated pipeline. In this system, image acquisition is user-driven, while subsequent steps—including preprocessing, patch generation, and model inference—are automated. This design allows for potential applications in near-real-time operational monitoring. Our study demonstrates that deep learning models enhance burned-area mapping performance. In addition, the combination of SAR-derived indices with log-ratio features further improves accuracy, illustrating the advantages of integrating advanced model architectures and combined input features into operational workflows. However, SAR-based mapping still trails behind optical-based approaches because of inherent noise and estimation uncertainty (Tanase et al., 2015). Our results indicate the feasibility of applying existing segmentation architectures to Sentinel-1 data, and we suggest that operational performance could be enhanced through a model-driven neural network design, improved handling of class imbalance, and richer input feature representations, such as using polarimetric decomposition and soil moisture. The present study represents a significant step toward advancing SAR-based burned-area mapping and its potential integration into operational services, especially in scenarios where cloud cover restricts the use of optical imagery. To facilitate the generalization and reproducibility of the proposed approach as well as its operational use, the source codes and data are available at https://github.com/sohel-raana/U-shaped-DL-SAR-BA.

6. Conclusion

Our study aimed to investigate the effectiveness of radar vegetation indices alongside a comprehensive analysis of U-shaped architecture-based methods for mapping burned areas using Sentinel-1 SAR data. Our findings revealed several significant insights into the application of these methodologies. The study demonstrates that radar-based vegetation indices (RVI and RFDI) can effectively delineate burned areas, performing similarly to Log-ratio and, in most instances, surpassing it within deep learning model frameworks. However, combining the log-ratio with vegetation indices are more suitable as they outperform other schemes among themselves. Notably, among the U-Net shaped models, U-Net++ exhibited superior performance when combining with log-ratio. And then after further investigation of input scheme and loss-function, it is found that scheme of log-ratio and indices with combined dice and focal loss and using U-Net++ architecture can perform best with an F1-score of 0.8364 and total IoU score of 0.7188. The effectiveness of radar vegetation indices suggests their potential integration into existing burned area monitoring systems, particularly in regions where log-ratio has discernable responses. Future research should explore model-driven neural network design, and auxiliary data integration to further enhance the accuracy and reliability of burned area mapping using SAR data.

CRediT authorship contribution statement

S.M. Sohel Rana: Writing – original draft, Visualization, Validation, Methodology, Investigation, Formal analysis. **Jaese Lee:** Writing – review & editing, Methodology, Data curation, Conceptualization. **Yoojin Kang:** Writing – review & editing, Methodology, Data curation. **Jungho Im:** Writing – review & editing, Supervision, Methodology, Funding acquisition, Conceptualization.

Declaration of competing interest

The authors declare that they have no known competing financial interests or personal relationships that could have appeared to influence the work reported in this paper.

Acknowledgement

This work was supported by the National Research Foundation of Korea (NRF) grant funded by the Korea government (MSIT) (No. NRF-2021R1A2C2008561), by Institute of Information & communications Technology Planning & Evaluation (IITP) grant funded by the Korea government (MSIT) (No. RS-2020-II201336, Artificial Intelligence Graduate School Program (UNIST)), and by the Korea Institute of Marine Science & Technology (KIMST) funded by the Ministry of Oceans and Fisheries (RS-2023-00256330).

Appendix A. Supplementary data

Supplementary data to this article can be found online at https://doi.org/10.1016/j.jag.2026.105141.

Data availability

Data will be made available on request.

References

Alvarez-Mozos, J., Villanueva, J., Arias, M., Gonzalez-Audicana, M., 2021. Correlation between NDVI and Sentinel-1 Derived Features for Maize. IEEE Int. Geosci. Remote Sens. Symp. (IGARSS) 6773–6776.

Badrinarayanan, V., Kendall, A., Cipolla, R., 2017. SegNet: a Deep Convolutional Encoder-Decoder Architecture for image Segmentation. IEEE Trans. Pattern Anal. Mach. Intell. 39, 2481–2495.

Ban, Y., Zhang, P., Nascetti, A., Bevington, A.R., Wulder, M.A., 2020. Near Real-Time Wildfire Progression Monitoring with Sentinel-1 SAR Time Series and Deep Learning. Sci. Rep. 10.

Bauer-Marschallinger, B., Paulik, C., Hochstöger, S., Mistelbauer, T., Modanesi, S., Ciabatta, L., Massari, C., Brocca, L., Wagner, W., 2018. Soil moisture from fusion of scatterometer and SAR: closing the scale gap with temporal filtering. Remote Sens. 10, 1030.

Belenguer-Plomer, M.A., Tanase, M.A., Chuvieco, E., Bovolo, F., 2021. CNN-based burned area mapping using radar and optical data. Remote Sens. Environ. 260, 112468.

Boschetti, L., Flasse, S.P., Brivio, P.A., 2004. Analysis of the conflict between omission and commission in low spatial resolution dichotomic thematic products: the Pareto Boundary. Remote Sens. Environ. 91, 280–292.

Bourgeau-Chavez, L.L., Kasischke, E.S., Brunzell, S., Mudd, J.P., Tukman, M., 2002. Mapping fire scars in global boreal forests using imaging radar data. Int. J. Remote Sens. 23, 4211–4234.

Bowman, D.M., Balch, J.K., Artaxo, P., Bond, W.J., Carlson, J.M., Cochrane, M.A., d'Antonio, C.M., DeFries, R.S., Doyle, J.C., Harrison, S.P., 2009. Fire in the Earth system. Science 324, 481–484.

Bowman, D.M.J.S., Kolden, C.A., Abatzoglou, J.T., Johnston, F.H., Van Der Werf, G.R., Flannigan, M., 2020. Vegetation fires in the Anthropocene. Nat. Rev. Earth Environ. 1, 500–515.

Chang, J.G., Shoshany, M., Oh, Y., 2018. Polarimetric Radar Vegetation Index for Biomass Estimation in Desert Fringe Ecosystems. IEEE Trans. Geosci. Remote Sens. 56, 7102–7108.

Chuvieco, E., Mouillot, F., Van der Werf, G.R., San Miguel, J., Tanase, M., Koutsias, N., García, M., Yebra, M., Padilla, M., Gitas, I., 2019. Historical background and current developments for mapping burned area from satellite Earth observation. Remote Sens. Environ. 225, 45–64.

Dang, K.B., Nguyen, C.Q., Tran, Q.C., Nguyen, H., Nguyen, T.T., Nguyen, D.A., Tran, T. H., Bui, P.T., Giang, T.L., Nguyen, D.A., Lenh, T.A., Ngo, V.L., Yasir, M., Nguyen, T. T., Ngo, H.H., 2024. Comparison between U-shaped structural deep learning models to detect landslide traces. Sci. Total Environ. 912, 169113.

De Luca, G., Silva, J.M., Modica, G., 2021. A workflow based on Sentinel-1 SAR data and open-source algorithms for unsupervised burned area detection in Mediterranean ecosystems. GISci. Remote Sens. 58, 516–541.

Dostalova, A., Navacchi, C., Greimeister-Pfeil, I., Small, D., Wagner, W., 2022. The effects of radiometric terrain flattening on SAR-based forest mapping and classification. Remote Sens. Lett. 13, 855–864.

Engelbrecht, J., Theron, A., Vhengani, L., Kemp, J., 2017. A simple normalized difference approach to burnt area mapping using multi-polarisation C-Band SAR. Remote Sens. 9, 764.

Ghosh, B., Garg, S., Motagh, M., Martinis, S., 2024. Automatic Flood Detection from Sentinel-1 Data using a Nested UNet Model and a NASA Benchmark Dataset. PFG –. J. Photogramm. Remote Sens. Geoinf. Sci. 92, 1–18.
Goutte, C., Gaussier, E., 2005. A Probabilistic Interpretation of Precision, recall and F-Score, with Implication for Evaluation. Lect. Notes Comput. Sci 345–359.
Huang, H., Lin, L., Tong, R., Hu, H., Zhang, Q., Iwamoto, Y., Han, X., Chen, Y.-W., Wu, J., 2020. Unet 3+: a full-scale connected unet for medical image segmentation. Proc. IEEE Int. Conf. Acoust. Speech Signal Process. ICASSP, 1055–1059.
Jenkins, M.A., Klein, R.N., McDaniel, V.L., 2011. Yellow pine regeneration as a function of fire severity and post-burn stand structure in the southern Appalachian Mountains. For. Ecol. Manage. 262, 681–691.
Jiang, C., Zhang, H., Wang, C., Ge, J., Wu, F., 2022. Water Surface Mapping from Sentinel-1 Imagery based on Attention-UNet3+: a Case Study of Poyang Lake Region. Remote Sens. 14, 4708.
Jin, Y., Randerson, J.T., Goetz, S.J., Beck, P.S., Loranty, M.M., Goulden, M.L., 2012. The influence of burn severity on postfire vegetation recovery and albedo change during early succession in north American boreal forests. J. Geophys. Res, Biogeosci, p. 117.
John, D., Zhang, C., 2022. An attention-based U-Net for detecting deforestation within satellite sensor imagery. Int. J. Appl. Earth Obs. Geoinf. 107, 102685.
Keeley, J.E., Bond, W.J., Bradstock, R.A., Pausas, J.G., Rundel, P.W., 2011. Fire in Mediterranean ecosystems: ecology, evolution and management. Cambridge Univ. Press.
Key, C.H., Benson, N.C., 2006. Landscape assessment (LA). In: Lutes, D.C., Keane, R.E., Caratti, J.F., Key, C.H., Benson, N.C., Sutherland, S., Gangi, L.J. (Eds.), 2006. FIREMON: Fire Effects Monitoring and Inventory System. Gen. Tech. Rep. RMRS-GTR-164-CD. US Department of Agriculture, Forest Service, Rocky Mountain Research Station, Fort Collins, CO p. LA-1-55, 164.
Kingma, D.P., Ba Adam, J.L., 2015. A method for stochastic optimization. In: 3rd International Conference on Learning Representations, ICLR 2015 - Conference Track Proceedings.
Kobayashi, S., Fujita, M.S., Omura, Y., Matthews, J.P., 2024. Analysis of the relationship between L-band SAR backscatter and understory weed density in eucalyptus plantation forests. Gisci. Remote Sens. 61, 2360771.
Kondylatos, S., Prapas, I., Ronco, M., Papoutsis, I., Camps-Valls, G., Piles, M., Fernández-Torres, M.Á., Carvalhais, N., 2022. Wildfire Danger Prediction and Understanding with Deep Learning. Geophys. Res, Lett, p. 49.
Kurum, M., 2015. C-band SAR backscatter evaluation of 2008 Gallipoli forest fire. IEEE Geosci. Remote Sens. Lett. 12, 1091–1095.
Lee, D., Son, S., Bae, J., Park, S., Lee, S., Seo, J., Kim, Y., Choi, M., Lee, Y., Kim, J., 2024. Enhancing wildfire damage detection performance with Swin Transformer using PlanetScope and Sentinel-2 satellite imagery: Analysis of multi-source data fusion. Korean J. Remote Sens. 40, 991–1004.
Lee, K., Kim, B., Park, S., 2023. Evaluating the potential of burn severity mapping and transferability of Copernicus EMS data using Sentinel-2 imagery and machine learning approaches. Gisci. Remote Sens. 60, 2192157.
Li, K., Xu, E., 2023. Differentiating effects of salvage logging and recovery patterns on post-fire boreal forests in Northeast China using a modified forest disturbance index. Gisci. Remote Sens. 60, 2188674.
Luft, H., Schillaci, C., Ceccherini, G., Vieira, D., Lipani, A., 2022. Deep Learning based Burnt Area Mapping using Sentinel 1 for the Santa Cruz Mountains Lightning complex (CZU) and Creek fires 2020. Fire 5, 163.
Niu, C., Gao, O., Lu, W., Liu, W., Lai, T., 2022. Reg-SA–UNet++: a lightweight landslide detection network based on single-temporal images captured postlandslide. IEEE J. Sel. Top. Appl. Earth Obs. Remote Sens. 15, 9746–9759.
Oktay, O., 2018. Attention U-Net: Learning where to look for the pancreas. arXiv preprint arXiv:1804.03999.
Padilla, M., Stehman, S.V., Ramo, R., Corti, D., Hantson, S., Oliva, P., Alonso-Canas, I., Bradley, A.V., Tansey, K., Mota, B., 2015. Comparing the accuracies of remote sensing global burned area products using stratified random sampling and estimation. Remote Sens. Environ. 160, 114–121.
Paluba, D., Papale, L.G., Laštovička, J., Perivolioti, T.M., Kalaitzis, P., Mouratidis, A., Karadimou, G., Štych, P., 2024. Tracking burned area progression in an unsupervised manner using Sentinel-1 SAR data in Google Earth Engine. IEEE J. Selected Topics Appl. Earth Obser. Rem. Sens.
Pausas, J.G., Keeley, J.E., 2009. A burning story: the role of fire in the history of life. Bioscience 59, 593–601.
Pechony, O., Shindell, D.T., 2010. Driving forces of global wildfires over the past millennium and the forthcoming century. PNAS 107, 19167–19170.
Periasamy, S., 2018. Significance of dual polarimetric synthetic aperture radar in biomass retrieval: an attempt on Sentinel-1. Remote Sens. Environ. 217, 537–549.
Quintano, C., Fernández-Manso, A., Fernández-Manso, O., 2018. Combination of Landsat and Sentinel-2 MSI data for initial assessing of burn severity. Int. J. Appl. Earth Obs. Geoinf. 64, 221–225.
Radman, A., Shah-Hosseini, R., Homayouni, S., 2023. A deep convolutional neural network for burn progression mapping using Sentinel-1 SAR time-series. Int. J. Remote Sens. 44, 2196–2215.
Ramayanti, S., Kim, B., Park, S., Lee, C.-W., 2024. Wildfire susceptibility mapping by incorporating damage proxy maps, differenced normalized burn ratio, and deep learning algorithms based on Sentinel-1/2 data: a case study on Maui Island. Hawaii. Gisci. Remote Sens. 61, 2353982.
Ronneberger, O., Fischer, P., Brox, T., 2015. U-Net: Convolutional Networks for Biomedical image Segmentation. Lect. Notes Comput. Sci 234–241.
Ruiz-Ramos, J., Marino, A., Boardman, C.P., 2018. Using Sentinel-1 SAR for monitoring long term variation in burnt forest areas. IEEE Int. Geosci. Remote Sens. Symp. (IGARSS) 4901–4904.
Seo, Y., Youn, Y., Kim, S., Kang, J., Jeong, Y., Choi, S., Im, Y., Lee, Y., 2023. Detection of Wildfire burned areas in California using Deep Learning and Landsat 8 Images. Korean J. Remote Sens. 39, 1413–1425.
Sudmanns, M., Tiede, D., Augustin, H., Lang, S., 2019. Assessing global Sentinel-2 coverage dynamics and data availability for operational Earth observation (EO) applications using the EO-Compass. Int. J. Digit. Earth.
Tanase, M.A., Kennedy, R., Aponte, C., 2015. Radar Burn Ratio for fire severity estimation at canopy level: an example for temperate forests. Remote Sens. Environ. 170, 14–31.
Tanase, M.A., Santoro, M., Wegmüller, U., de la Riva, J., Pérez-Cabello, F., 2010. Properties of X-, C- and L-band repeat-pass interferometric SAR coherence in Mediterranean pine forests affected by fires. Remote Sens. Environ. 114, 2182–2194.
Torres, R., Davidson, M., 2019. Overview of Copernicus SAR space component and its evolution. IEEE Int. Geosci. Remote Sens. Symp. (IGARSS) 5381–5384.
Van der Werf, G.R., Randerson, J.T., Giglio, L., Collatz, G., Mu, M., Kasibhatla, P.S., Morton, D.C., DeFries, R., Jin, Y.v., van Leeuwen, T.T., 2010. Global fire emissions and the contribution of deforestation, savanna, forest, agricultural, and peat fires (1997–2009). Atmos. Chem. Phys. 10, 11707–11735.
Verhegghen, A., Eva, H., Ceccherini, G., Achard, F., Gond, V., Gourlet-Fleury, S., Cerutti, P.O., 2016. The potential of Sentinel satellites for burnt area mapping and monitoring in the Congo Basin forests. Remote Sens. 8, 986.
Zhang, P., Ban, Y., Nascetti, A., 2021. Learning U-Net without forgetting for near real-time wildfire monitoring by the fusion of SAR and optical time series. Rem. Sens. Environ. 261, 112467.
Zhang, P., Ban, Y., Nascetti, A., 2023. Total-variation regularized U-Net for wildfire burned area mapping based on Sentinel-1 C-Band SAR backscattering data. ISPRS J. Photogramm. Remote Sens. 203, 301–313.
Zhang, P., Hu, X., Ban, Y., Nascetti, A., Gong, M., 2024. Assessing Sentinel-2, Sentinel-1, and ALOS-2 PALSAR-2 Data for Large-Scale Wildfire-burned Area Mapping: Insights from the 2017–2019 Canada Wildfires. Remote Sens. 16, 556.
Zhang, P., Nascetti, A., Ban, Y., Gong, M., 2019. An implicit radar convolutional burn index for burnt area mapping with Sentinel-1 C-band SAR data. ISPRS J. Photogramm. Remote Sens. 158, 50–62.
Zhou, Z., Siddiquee, M.M.R., Tajbakhsh, N., Liang, J., 2019. Unet++: Redesigning skip connections to exploit multiscale features in image segmentation. IEEE Trans. Med. Imaging 39, 1856–1867.